

ORIGINAL RESEARCH ARTICLE

Characterization of triply periodic minimal surface structures obtained using toolpath-based construction design

Shujie Tan¹, Xi Zhang¹, Ziyu Wang¹, Liping Ding¹, Wenliang Chen¹,
Yicha Zhang^{2*}

¹College of Mechanical and Electrical Engineering, Nanjing University of Aeronautics and Astronautics, Nanjing, P. R. China

²ICB-COMM, UMR 6303, CNRS, Univ. Bourgogne Franche-Comté, UTBM, Belfort, France

Abstract

Triply periodic minimal surface (TPMS) cellular structures of Ti6Al4V with theoretically calculated relative densities ranging from 4% to 22.6% were designed using a toolpath-based construction method and fabricated by laser powder bed fusion, and their macrostructure, microstructure, and compression performance were investigated. The results indicated that the macrostructure was the same as that of TPMS structures designed using the traditional method. In contrast, the microstructures of the as-built samples and the samples after stress-relief annealing were slightly different from those of the traditional ones. Moreover, compression test results of the Schwarz-P structures showed that the compressive modulus was positively related to the calculated relative density, and a Gibson-Ashby model was established to quantitatively describe the relationship between the compressive modulus and theoretical relative density. The findings of this work show that the mechanical performance of a TPMS structure obtained using a toolpath-based construction design can be accurately predicted using geometric parameters or printing toolpaths. This will be helpful during the design stage.

Keywords: Additive manufacturing; Compression test; Laser powder bed fusion; Toolpath-based construction design; Triply periodic minimal surface structure

***Corresponding author:**

Yicha Zhang
(yicha.zhang@utbm.fr)

Citation: Tan S, Zhang X, Wang Z, et al., 2022, Characterization of triply periodic minimal surface structures obtained using toolpath-based construction design. *Mater Sci Add Manuf.* 1(3): 17.
<https://doi.org/10.18063/msam.v1i3.17>

Received: July 31, 2022

Accepted: September 5, 2022

Published Online: September 21, 2022

Copyright: © 2022 Author(s). This is an Open Access article distributed under the terms of the Creative Commons Attribution License, permitting distribution, and reproduction in any medium, provided the original work is properly cited.

Publisher's Note: Whioce Publishing remains neutral with regard to jurisdictional claims in published maps and institutional affiliations.

1. Introduction

At present, additive manufacturing (AM), especially the powder bed fusion (PBF) process, plays an important role in the biomedical, aerospace, automotive, and heat exchanger manufacturing industries^[1-3]. Due to its ability to fabricate freeform surfaces, AM greatly expands design freedom. In industry, an increasing number of components with extremely complex shapes, such as lattices, Voronoi foam, triply periodic minimal surfaces (TPMSs), and topological shapes, have been designed, fabricated, and applied^[4,5] because of their excellent physical and mechanical properties. Researchers have also focused on the design methods^[6,7], manufacturing evaluation^[8,9], and performance^[10,11] of these structures with complex shapes. However, according to the literature and our own studies, there are at least three unsolved problems in the manufacturing chain when

using laser PBF (LPBF) to manufacture such structures on an industrial scale. The first is the limitations of the stereolithography (STL) file format. It is difficult and time-consuming for commercial pre-processing software (i.e., Magics, Voxel Dance, and P3Ds) to handle the STL model of lattice/cellular structures created by scholars using the proposed novel design methods when the number of structural units exceeds ten thousand or more. Second, it is difficult to evaluate the manufacturability and manufacturing results of such complex structures because traditional evaluation methods are unsuitable for AM processes^[8]. Finally, the performance (i.e., physical and mechanical properties, and failure mechanism) of such novel structures is still unclear, although many scholars have focused on this topic.

To solve the first problem, Ding *et al.*^[12] proposed an STL-free design and manufacturing paradigm for high-precision PBF, and Feng *et al.*^[13,14] proposed an efficient generation strategy for hierarchical porous scaffolds with freeform external geometries. Both groups simplified the three-dimensional (3D) calculations to two-dimensional (2D) operations to improve the calculation efficiency. However, the infilling efficiency remains a problem. Similar to this simplified method, we proposed a toolpath-based construction method for designing and printing porous structures in a previous study^[15]. In our method, we used a toolpath pattern to infill the hull model, directly generating the toolpath of the porous structure. Compared with the traditional pre-processing method, the toolpath-based construction method exhibits a significant advantage in terms of toolpath precision and generating efficiency.

However, as mentioned above, to apply cellular structures generated by toolpath-based construction on an industrial scale, the manufacturability/manufacturing results and structural performance still need to be investigated. Although we analyzed the manufacturability of a cellular structure generated using the toolpath-based construction method and developed a manufacturability predictor for these structures in previous papers^[15,16], we did not investigate the performance of structures generated by the toolpath-based method.

Yan *et al.*^[17] evaluated the manufacturability and performance of LPBF-produced TPMS gyroid lattice structures. They found that the yield strength and Young's modulus of the gyroid lattice structures increased with decreasing unit cell size because of the denser struts of the lattice structures with smaller unit cell sizes. In another study, Yan *et al.*^[18] established two equations based on the Gibson-Ashby model to predict the compression properties of the 316L stainless steel gyroid lattice structures; however, there were differences between the

experimentally tested values and the values predicated by the Gibson-Ashby model. Many other scholars have investigated the microstructure and mechanical deformation behavior of LPBF-produced lattice structures. However, to the best of our knowledge, all of these studies used the conventional AM data-processing method when printing the lattice structure. As pointed out by Neikter *et al.*^[19], the microstructure of LPBF-produced samples is related to the laser scanning strategy, that is, the toolpath. However, the toolpath generated by the toolpath-based construction method is different from that generated by commercial AM data pre-processing software. Hence, it is unknown whether the performance of a lattice structure fabricated using toolpath-based construction design is the same as that of the traditionally designed structures.

In summary, there is a gap in knowledge regarding the microstructure and mechanical performance of lattice structures obtained using toolpath-based design. To fill this gap, we fabricated a TPMS Schwarz-P structure using our proposed method and investigated its microstructure and mechanical performance. The rest of the paper is organized as follows: Section 2 introduces the experimental materials and methods, Section 3 gives the experimental results and discusses the results, and we conclude with Section 4.

2. Materials and methods

2.1. TPMS Schwarz-P surface

A TPMS is an implicit surface with zero mean curvature^[3]. Owing to their smooth surfaces and highly interconnected porous architectures, TPMS structures have been applied in many domains. The Schwarz-P surface is a typical type of TPMS. Equation 1 gives its mathematical expression, and Figure 1 shows Schwarz-P surfaces with different unit sizes and shape factors.

$$\varphi_P(x, y, z) : \cos \frac{2\pi}{k} x + \cos \frac{2\pi}{k} y + \cos \frac{2\pi}{k} z = c \quad (1)$$

2.2. Toolpath-based construction method

In this study, a toolpath-based construction method was used to construct and generate printing toolpaths for the TPMS-Schwarz-P structures. Figure 2 shows the workflow of the printing toolpath generation of the TPMS-Schwarz-P structure through the toolpath-based construction method. The hull model, AM parameters, and mathematical equation of the Schwarz-P surface and its corresponding toolpath pattern were used as the input variables in this method. As shown in Figure 2, the box model was first sliced at a fixed thickness to obtain the layer contours. Then, the layer contours were used to construct the polygons to be infilled. Finally, the polygons

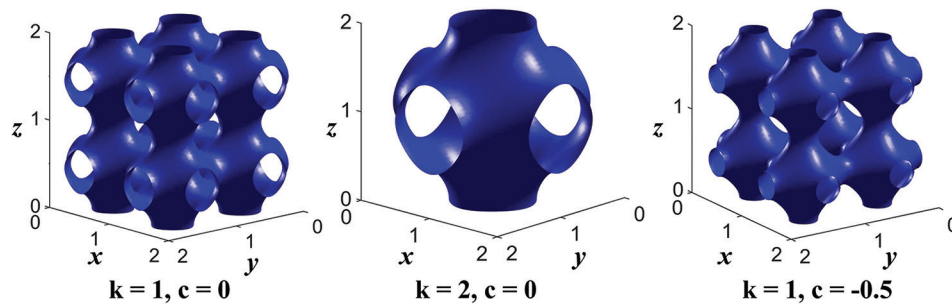


Figure 1. Schwarz-P surface with different parameters.

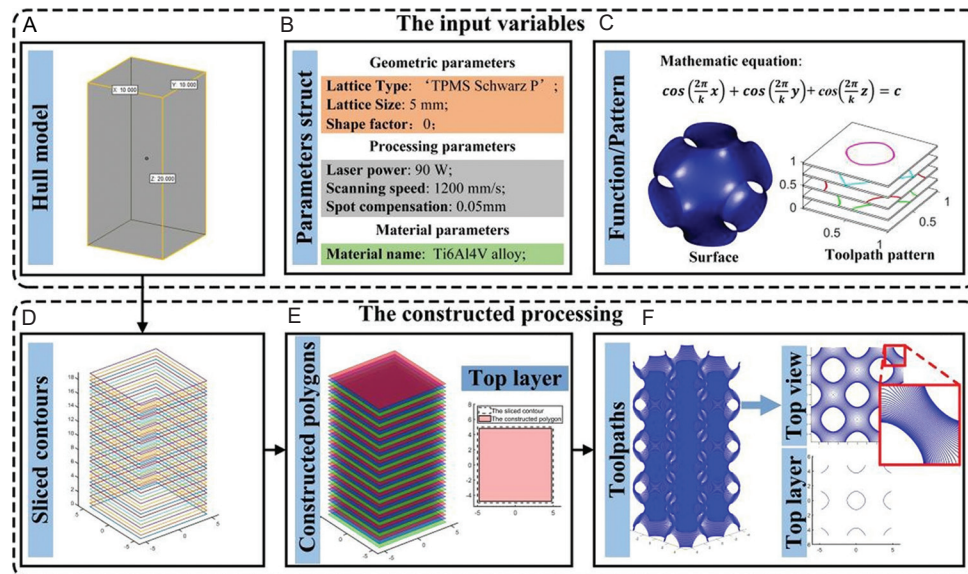


Figure 2. Workflow of the toolpath-based construction method.

were infilled using the Schwarz-P toolpath pattern. More details about the toolpath-based construction method can be found in our previous studies^[20,21].

Figure 3 exhibits the STL model of TPMS Schwarz-P structure, and its printing toolpaths generated by different methods. According to Figure 3, our observations are as follows: (i) the toolpaths generated by our method are smoother than those generated by Magics; and (ii) the toolpaths generated by Magics contain closed contours whether the thin wall optimization is selected. In this case, the wall thickness of the structure depended on the contours and their processing parameters. Opposite to Magics, our method used single-curve rather than contour as the printing toolpath. For this single-toolpath structure obtained through the toolpath-based construction method, the wall thickness was determined by the processing parameters, that is, the laser power and scanning speed. Without any hatching in the toolpath, the microstructure and mechanical performance of this Schwarz-P structure

differed slightly from those of the CAD model-based structure.

2.3. LPBF processing and materials

Gas-atomized Ti6Al4V powder supplied by ZhongHangMaiTe (China) was selected as the raw material in this study. Figure 4A presents the spherical morphology of the Ti6Al4V powder, and Table 1 lists the chemical composition. The size distributions were $D_{10} = 18.6 \mu\text{m}$, $D_{50} = 34.3 \mu\text{m}$, and $D_{90} = 57.6 \mu\text{m}$. The Ti6Al4V Schwarz-P structures were printed on a 150-mm diameter titanium alloy substrate under an argon protective atmosphere using a commercial SLM printer (Ti150, Profeta, China). The Ti150 printer (Figure 4B) was equipped with an IPG Photonics fiber laser, delivering a maximum power of $P = 200 \text{ W}$ at $\lambda = 1064 \text{ nm}$ and having a laser spot size of $50 \mu\text{m}$.

Twenty-five samples ($10 \times 10 \times 20 \text{ mm}$) with different geometric parameters were fabricated for compression, and four samples ($10 \times 10 \times 5 \text{ mm}$) with the same

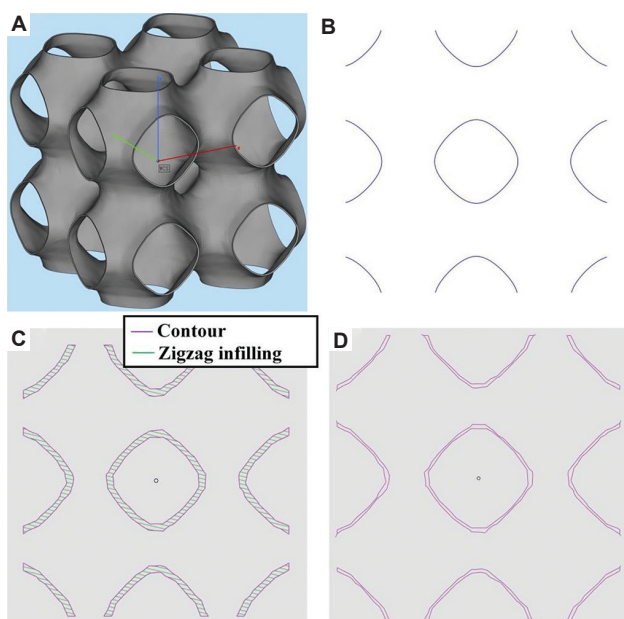


Figure 3. Model and its printing toolpaths generated by different methods. (A) STL model of TPMS Schwarz-P structure. Toolpaths generated by (B) our method, (C) Magics without spot compensation and thin-wall optimization, and (D) Magics with spot compensation and thin-wall optimization.

geometric parameters were fabricated for microstructural characterization. The samples were designated as A0-A0.8, B0-B0.8, C0-C0.8, D0-D0.8, E0-E0.8, and F1-F4. An illustration of the orientation, sample dimensions, and distribution within the substrate for these Schwarz-P structures is shown in Figure 5A. In this study, the laser power, scanning speed, and printing layer thickness were 90 W, 1100 mm/s, and 30 μm, respectively. The oxygen content was less than 0.1%. After printing, F1 and F3 were immediately cut by wire electrical discharge machining (WEDM), whereas the remaining samples were heat treated to relieve the residual thermal stress before cutting. Figure 5B illustrates the stress-relief heat treatment process. The geometric parameters and corresponding theoretical porosities are listed in Table 2. Here, we assumed that the width of the melt track would not change

Table 1. Composition of Ti6Al4V powder

Main ingredients	Ti	Al	V		
Content/%	Bal	5.50-6.75	3.50-4.50		
Minor ingredients	Fe	C	N	H	O
Content/%	≤ont	≤onte	≤onte	≤onten	≤ont

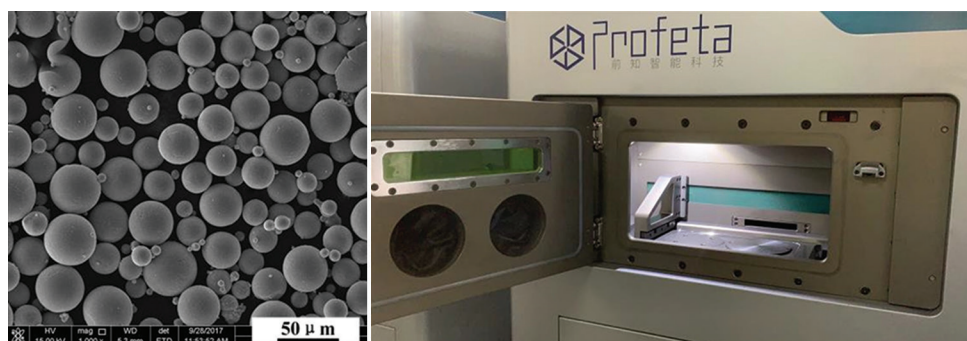


Figure 4. Material and Ti150 machine.

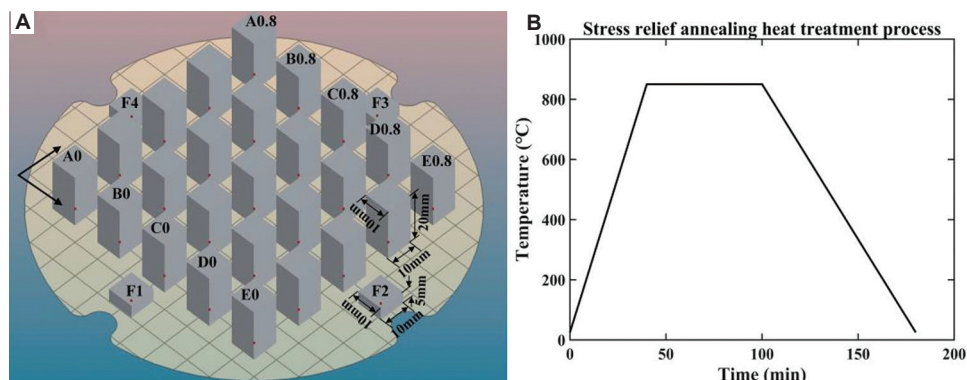


Figure 5. (A) An illustration of the orientation, sample dimensions, and distribution within the substrate for the fabricated samples. (B) An illustration of the stress relief heat treatment to the fabricated samples.

Table 2. The geometric parameters and processing parameters of the Schwarz-P structures

No.	Lattice size	Shape factor	Theoretical relative density
A0	1	0	0.2262
A0.2	1	0.2	0.2244
A0.4	1	0.4	0.2201
A0.6	1	0.6	0.2124
A0.8	1	0.8	0.2003
B0	2	0	0.1130
B0.2	2	0.2	0.1122
B0.4	2	0.4	0.1101
B0.6	2	0.6	0.1062
B0.8	2	0.8	0.1001
C0	3	0	0.0712
C0.2	3	0.2	0.0719
C0.4	3	0.4	0.0725
C0.6	3	0.6	0.0735
C0.8	3	0.8	0.0710
D0	4	0	0.0565
D0.2	4	0.2	0.0561
D0.4	4	0.4	0.0550
D0.6	4	0.6	0.0531
D0.8	4	0.8	0.0501
E0	5	0	0.0452
E0.2	5	0.2	0.0449
E0.4	5	0.4	0.0440
E0.6	5	0.6	0.0425
E0.8	5	0.8	0.0401
F1-F4	1	0	0.2262

when the processing parameters remained the same. We also considered the cross-sectional shape of the melt track to be a rectangle and neglected the overlap in the corner. Under this assumption, the theoretical relative density of the Schwarz-P structure with no hatched toolpath was calculated as follows:

$$d_{tr} = \frac{\rho_p}{\rho_s} = \frac{w \times h \times \sum len_i}{V} \quad (II)$$

Where d_{tr} is the theoretical relative density of the Schwarz-P structure, w is the width of the melt track, h is the layer thickness, len_i is the length of the i th toolpath, and V is the volume of the hull model of the Schwarz-P structure. In this study, the layer thickness h is 0.03mm, and the melt track width w is 0.12 mm when laser power, scanning speed and laser spot diameter are 90 W, 1100 mm/s and 50 μ m, respectively.

2.4. Material characterization and mechanical properties

The macrostructure of the Schwarz-P structures (A0-E0.8) was analyzed using optical microscopy (OM; HiROX RH-2000, Japan) and scanning electron microscopy (SEM). Electron backscatter diffraction (EBSD) was used to further analyze the grain structure and phase distribution of the remaining four samples (F1 – F4). The Schwarz-P samples for EBSD were mechanically polished and then argon ion-polished for 5 h at 4 kV voltage and 2 angles. The mass of each structure was measured using an analytical balance (BSS224S, Hengda, China), and the relative density d_{mr} was calculated as follows:

$$d_{mr} = \frac{m_p}{V \times \rho_s} \quad (III)$$

Where m_p is the mass of the Schwarz-P structure, V is the volume of the Schwarz-P structure, and $\rho_s = 4.43\text{g/cm}^3$ is the density of the dense Ti6Al4V alloy.

Static uniaxial compression experiments were performed using a cmt5305 machine based on the ISO 13314:2011 standard^[22]. Compression tests were conducted at room temperature at a constant rate of 2 mm/min. Three identical samples were tested for each Schwarz-P structure. After the test, the fracture surface morphology of each sample was examined using SEM.

According to the Gibson-Ashby model, mechanical properties are related to the relative density of open-cell porous structures^[23]. Equation IV gives the relationship between the elastic modulus and relative density.

$$\frac{E_p}{E_s} = C_1 \left(\frac{\rho_p}{\rho_s} \right)^{n_1} \quad (IV)$$

Where E_p is the elastic modulus of the porous structure, E_s is the elastic modulus of the bulk material, and for Ti6Al4V alloy, $E_s = 110$ GPa. ρ_p and ρ_s are the porous and dense material density, respectively. C_1 and n_1 are the coefficients and can be calculated by fitting the test results into Equation IV. Normally, C_1 is in the range of 0.1 to 4, and n_1 equals to 2. It must be pointed out that, compared with the real measured relative density, we thought that the theoretically calculated value is more suitable for Equation IV. The reason is detailed in section 3.1.

3. Results and discussion

3.1. Macrostructural analysis

Figures 6A–E present the manufacturing samples of Schwarz-P structures with different geometric parameters. Figures 6F–H show enlarged images of regions A1,

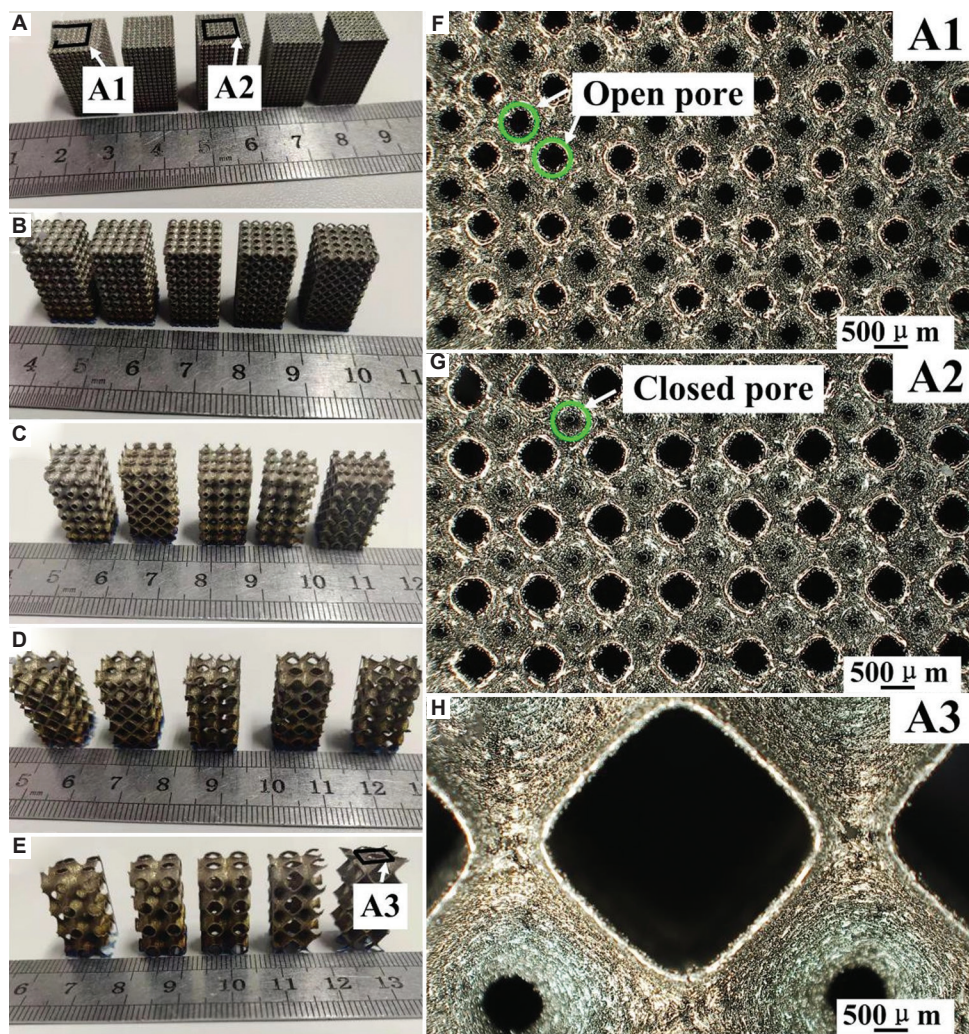


Figure 6. The manufacturing samples of Schwarz-P structures with different geometric parameters. (A) A0, A0.2, A0.4, A0.6, A0.8. (B) B0, B0.2, B0.4, B0.6, B0.8. (C) C0, C0.2, C0.4, C0.6, C0.8. (D) D0, D0.2, D0.4, D0.6, D0.8. (E) E0, E0.2, E0.4, E0.6, E0.8. (F), (G), and (H) show the enlarged images of regions A1, A2, and A3, respectively.

A2, and A3, respectively. As shown in Figure 6, all the Schwarz-P structures were successfully fabricated; however, inconsistent with the designs, several structures (A0.4, A0.6, and A0.8) had closed pores. Theoretically, the Schwarz-P surface divides the space into two independent regions; however, there is width to the melt track, and pores will close if the pore size is smaller than the width of the melt track, resulting in many closed cavities filled with unmelted powder particles. Typically, the width of the Ti6Al4V melt track at the given processing parameters in this study (laser power = 120 W, scanning speed = 1100 mm/s, layer thickness = 0.03 mm, and laser spot diameter = 0.05 mm) was 120 μm . However, as we found in our previous study^[15], this width increased significantly in the corner of the toolpath. The closed toolpath shown by the galvanometer scanning system was not a smooth curve with G2 continuous; rather, it was a

polyline with many corners/vertices. Hence, the width of the melt track of the small pore became much larger than we expected. Figure 7 depicts variations between the actual pore size and the designed geometric parameters of the Schwarz-P structure. As the shape factor increases, the minimal pore size decreases; in contrast, as the unit size increases, the minimal pore size increases. In addition, an interesting phenomenon, as shown in Figure 7), is that the structure had some broken holes, meaning that when the unit size was >5 mm, the Schwarz-P structure did not satisfy the AM constraints.

Figure 8 presents a comparison of the theoretical and measured relative densities of the Schwarz-P structures. As shown in the figure, except for samples A0.4, A0.6, and A0.8, the theoretically calculated results are consistent with the measured results. As shown in Figure 5, samples A0.4,

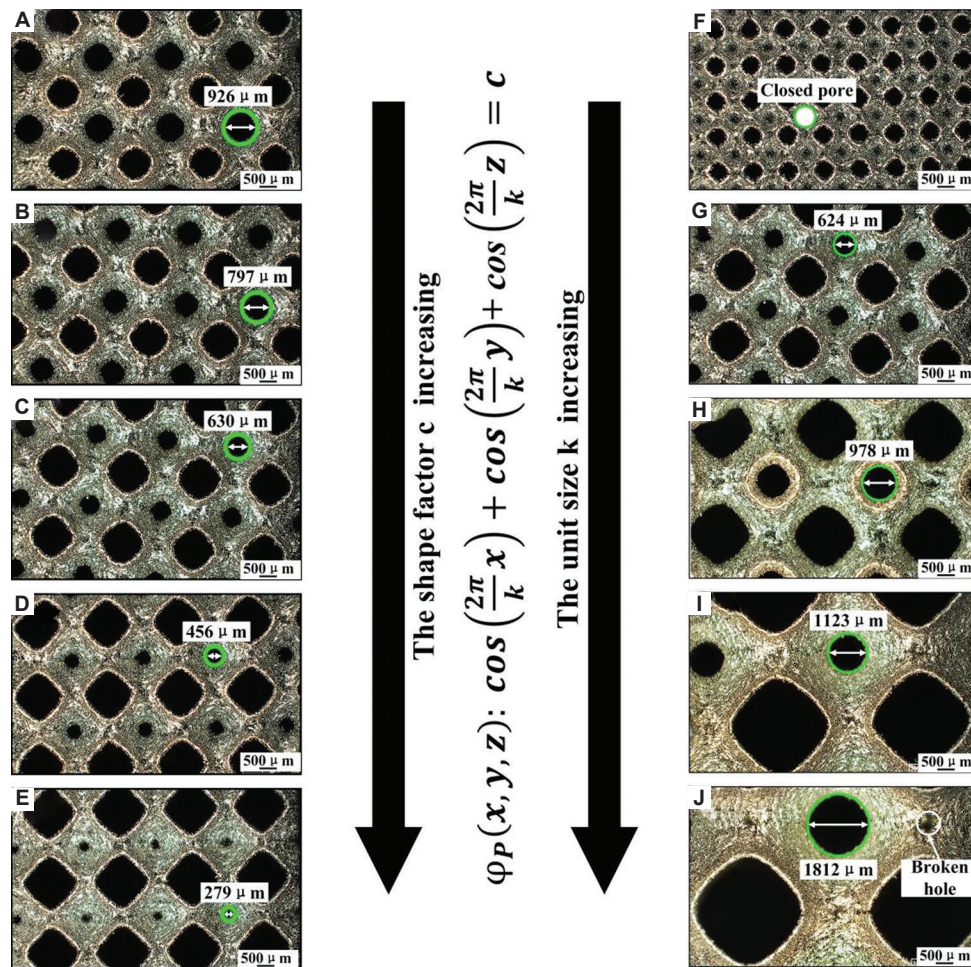


Figure 7. The variations between the real pore size and design geometric parameters of the Schwarz-P structure. (A-E) show the top views of samples B0, B0.2, B0.4, B0.6, and B0.8, respectively. (F-J) show the top views of samples A0.4, B0.4, C0.4, D0.4, and E0.4, respectively.

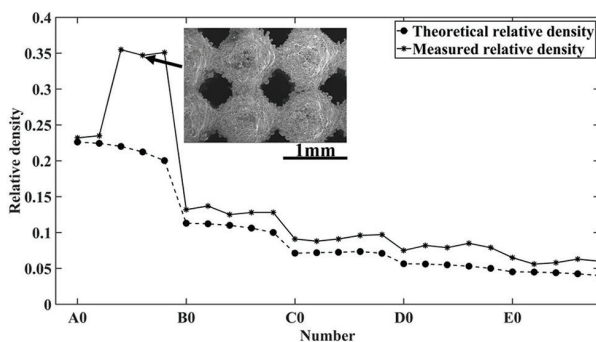


Figure 8. Comparing results of the theoretical and the measured relative density.

A0.6, and A0.8 had some closed cavities filled with unmelted powder particles, which is why the measured relative densities of these samples were much greater than the theoretically calculated results. In addition, the measured results were slightly greater than the theoretical results. This

is because some semi-melted powder became attached to the surface. However, when we calculated the theoretical relative density, we used the width of the polished samples, neglecting the attached powder. Moreover, on comparing the theoretical relative densities of samples A0, B0, C0, D0, and E0 (or other samples with the same shape factor but different unit sizes), it was found that when the shape factor remained constant, the theoretical relative density of the Schwarz structure decreased rapidly with increasing unit size. On comparing the theoretical relative densities of samples A0, A0.2, A0.4, A0.6, and A0.8 (or other samples with the same unit size and different shape factors), when the unit size remained constant, the theoretical relative density decreased with increasing shape factor; however, the change was very small and almost negligible.

Therefore, we considered that the measured relative density did not reflect the actual densification of the Schwarz-P structures because the partially melted and unmelted powder particles attached to the

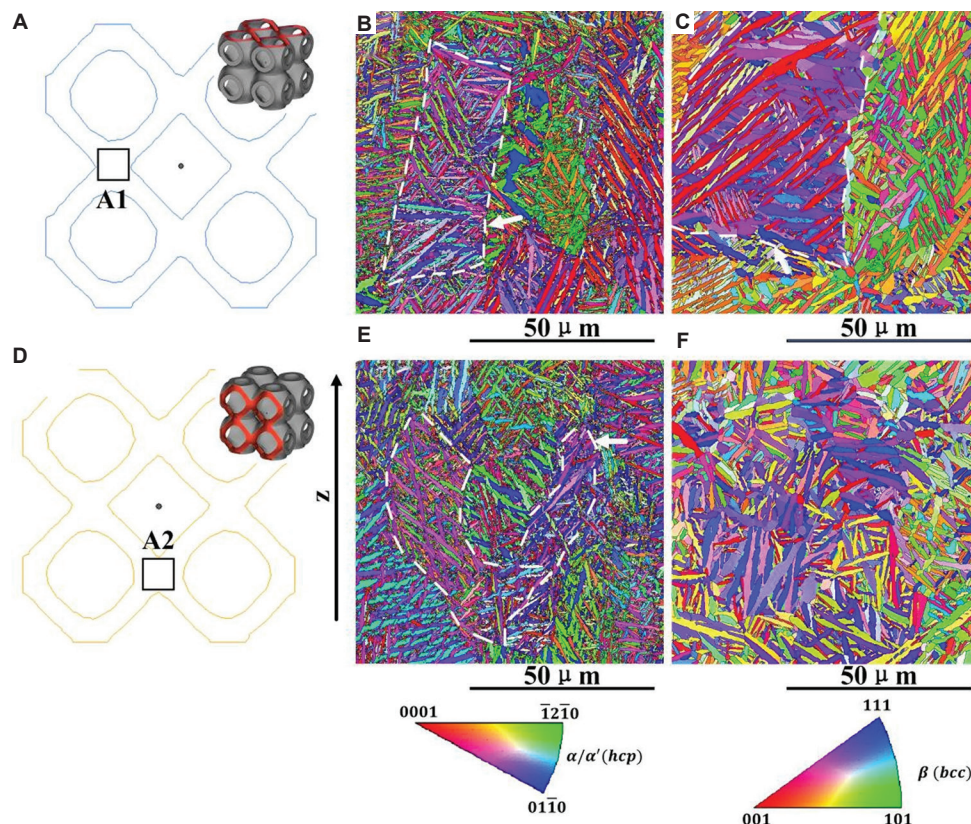


Figure 9. The EBSD orientation maps of the as-built and the heat treatment structures. (A) and (D) show the diagrams of the top and side scanning regions, respectively. (B) As-built structure, region A1. (C) Structure after stress relief heat treatment, region A1. (E) As-built structure, region A2. (F) Structure after stress relief heat treatment, region A2.

structural surface affected the measurement results. Hence, in the remainder of this study, the theoretically calculated relative density, instead of the measured value, was used.

3.2. Microstructure analysis

In general, the solidification of Ti6Al4V during printing process starts with the melted deposit, which consists of the liquid β phase. As reported by Zhao *et al.*^[24], due to the high cooling rates, further cooling leads to the transformation from the β phase to martensite phase (α') phase during the LPBF process. Figure 9A and D show the scanning regions of the EBSD maps, and Figure 9B and E and Figure 8C and F show the microstructures of the as-built and heat-treated Ti6Al4V samples, respectively. As shown in Figure 9B and E, the EBSD orientation maps of the as-built Ti6Al4V samples show that the original β grains and acicular α/α' within each β grain. The white dotted lines in the figures indicate the original β grain boundaries. Compared with the results reported by Chang *et al.*^[25] and Vrancken *et al.*^[26], the length of the original β grains in this study is smaller (approximately 25 μm). Meanwhile, as reported by Zhao *et al.*^[24], the original β columnar grains are parallel to

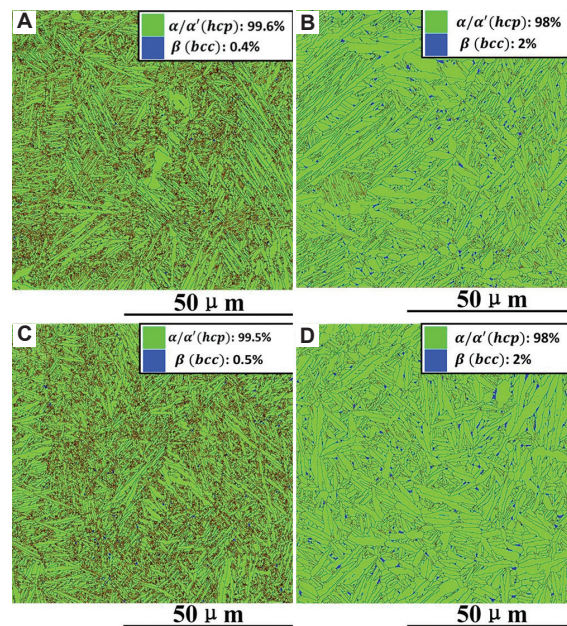


Figure 10. EBSD phase mapping of the LPBF-produced Schwarz-P structures. (A) and (C) show the phase mapping of region A1 and A2 in the as-built samples, respectively. (B) and (D) show the phase mapping of region A1 and A2 in the samples after stress relief heat treatment.

the build direction. However, as shown in Figure 9E, the orientation of the original β columnar grains was tilted, and this phenomenon is more obvious in the samples after heat treatment (Figure 9F).

Figure 10 shows the phase composition of the LPBF-produced Schwarz-P structures. As shown in Figure 9A and C, <0.5% body center β phase can be found in the as-built samples, while 2% β phase exists in the samples after stress relief heat treatment. The β phase is presented as a dot between the α/α' phase.

3.3. Mechanical performance behavior

Figure 11 shows the compressive modulus and maximum compressive stress of the Schwarz-P structures with different parameters. The structure with the largest elastic modulus is sample A0.6 (elastic modulus of 2.23 GPa), whereas that with the smallest elastic modulus is sample E0.2 (elastic modulus of 0.097 GPa). Similarly, the structure with the largest maximum compressive stress is sample A0.8 (maximum compressive stress of 101 MPa), whereas that with the smallest compressive stress is sample E0.2 (maximum compressive stress of 2.5 MPa). In addition, it can be seen from Figures 11A and B that when the shape factor was constant, the elastic modulus and maximum compressive stress of the Schwarz-P structure

decreased with increasing unit size. Meanwhile, when the unit size was constant, the elastic modulus and maximum compressive stress changed very little. Comparing these results with those mentioned in Section 3.1, it is apparent that the effect of the unit size and shape factor on the elastic modulus and maximum compressive stress is consistent with the effect on the theoretical relative density.

To quantitatively investigate the relationship between the elastic modulus and the theoretical relative density, the Gibson-Ashby model was used to describe the experimental results. As mentioned above, the coefficient $n1$ in the Gibson-Ashby model normally equals t for an open-cell structure. Two Gibson-Ashby equations were used to fit the results to better evaluate the elastic modulus of the Schwarz-P structure. As given by Equations V and VI, one has a fixed $n1 = 2$, whereas the other does not. Figure 12 presents the fitting plots based on Equations V and VI, which describe the relationship between the relative elastic modulus of the LPBF-produced Ti6Al4V Schwarz-P structure with respect to the theoretical relative density. Both Gibson-Ashby equations fit well. The first fitting line for the elastic modulus (line 1, marked red in Figure 12) gives the relationship $E_p/E_s = 0.31(\rho_p/\rho_s)^{1.76}$, with a fitting R^2 value of 0.9729, whereas the second fitting line for the elastic modulus (line 2, marked blue in Figure 12) gives the relationship $E_p/E_s = 0.56(\rho_p/\rho_s)^2$, with a fitting R^2 value of 0.9546. The results indicated that the revised model (Equation V) performed better than the commonly used model (Equation VI).

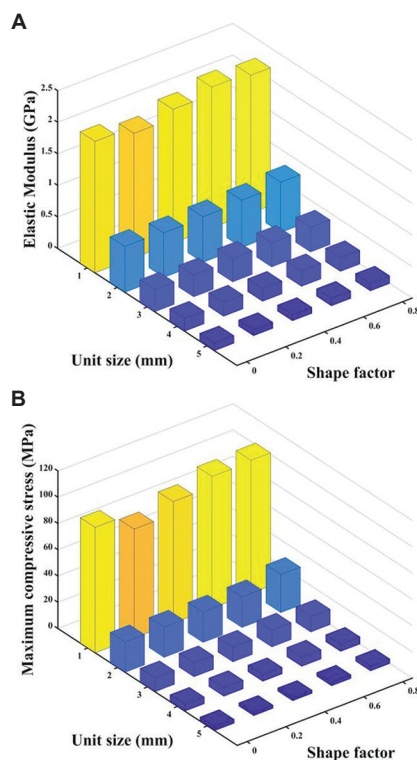


Figure 11. Compression modulus (A) and compressive stress (B) for Schwarz-P structures with different parameters.

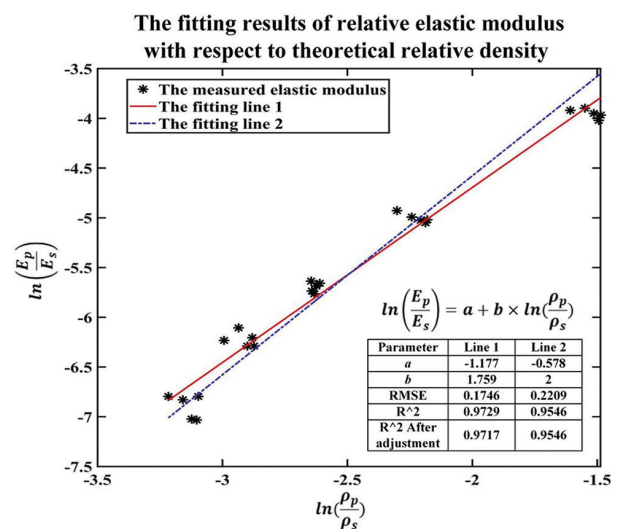


Figure 12. Fitting results of the compression modulus with respect to theoretical relative density for the Schwarz-P structures using the Gibson-Ashby model.

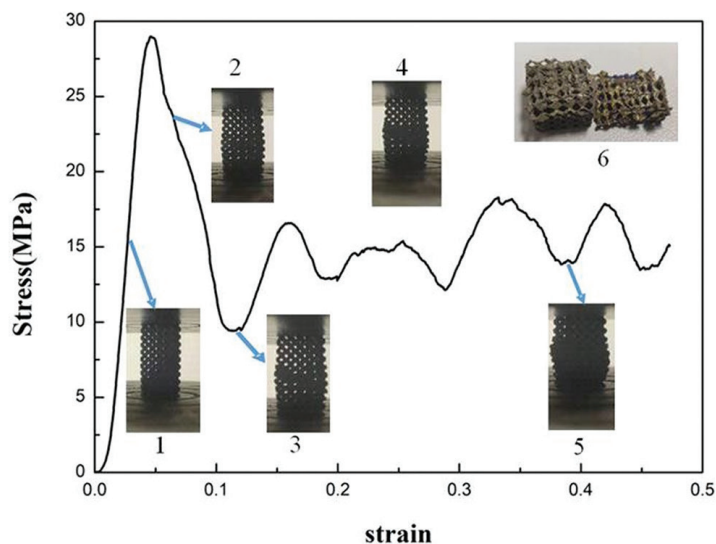


Figure 13. Deformation process of the Schwarz-P structure: sample B0.8.

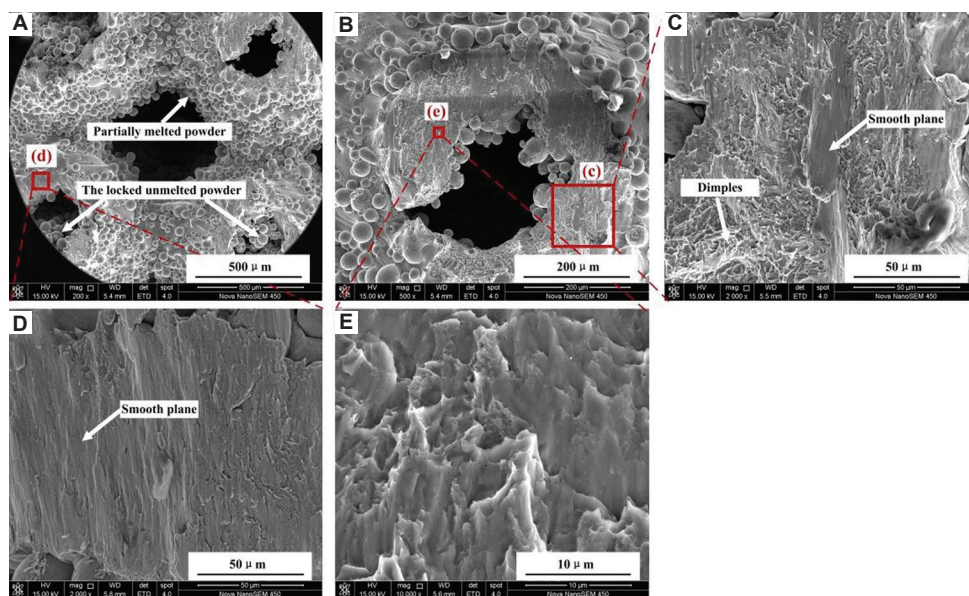


Figure 14. Fracture surface morphology of Schwarz-P structure: sample A0.6. (A) fracture macro-surface at a low magnification of $\times 200$. (B), (C), (D), and (E) show the fracture micro-surface at high magnification of $\times 500$, $\times 2000$, $\times 2000$, and $\times 10000$, respectively.

$$\ln\left(\frac{E_p}{E_s}\right) = \ln(C_1) + n_1 \times \ln\left(\frac{\rho_p}{\rho_s}\right) \quad (V)$$

$$\ln\left(\frac{E_p}{E_s}\right) = \ln(C_1) + 2\ln\left(\frac{\rho_p}{\rho_s}\right) \quad (VI)$$

3.4. Compression failure mechanism

To investigate the failure mechanism of the Schwarz-P structures, the crushing behavior of the samples was recorded, and a typical sample B0.8 was chosen to explain

the results. The results are shown in Figure 13. In general, the compression process had three stages:

- (i) Initial elastic stage. During this stage, as the compression displacement increased, the compressive stress increased rapidly until it reached the maximum value, but the strain changed slowly. The compressive strain and stress thus exhibited a linear relationship.
- (ii) Plastic plateau stage. During this stage, a localized bulging phenomenon began to occur in the middle region of the Schwarz-P structure (as shown in Figure 13, point 2). With further increases in the

compressive load, shear failure occurred at an incline angle of approximately 30° between the shear cracking propagation path and the compressive loading direction (as shown in Figure 13, points 3 – 5).

- (iii) Densification stage. Unfortunately, the samples slipped and fractured, and thus loading was not continued. Figure 13, point 6, presents the final fractured Schwarz-P structure. Figure 14 shows the morphologies of the fracture surface of sample A0.6 after the static compression test. Some partially melted powder particles are attached to the surface and some unmelted powder particles are locked in the cavities. The fractured surface consists of a mixture of smooth planes and micro-sized dimples, thus exhibiting a mixed ductile and brittle failure mode.

4. Conclusions

In this study, Schwarz-P cellular structures with unit sizes ranging from 1 mm to 5 mm and shape control factors ranging from 0 to 0.8 obtained using a toolpath-based construction design were fabricated by LPBF using Ti6Al4V powder. The macrostructure, microstructure, and compression performance of these structures were investigated. The main findings are summarized as follows:

- (i) The size of the open pores decreased as the shape control factor increased and increased as the unit size increased, which is consistent with the designs. However, when the unit size was 1 mm and the shape control factor was >0.4, the open pores became closed cavities, locking in unmelted powder particles. Similar to the conventional design, partially melted powder particles attached to the surface of the Schwarz-P structures were found.
- (ii) Except for structures with closed cavities, the relative densities of the Schwarz-P structures calculated using the toolpath and the melt track width were consistent with the measured values. When excluding the influence of unmelted and partially melted powder particles, the calculated relative density was more suitable for the prediction of mechanical properties.
- (iii) The EBSD maps indicated that the original β grains and acicular α' phase within each β grain together constituted the microstructure of the Ti6Al4V Schwarz-P structure, as reported in the literature; however, the original β grains in this study were smaller, and the orientation of the original β grains in the side surface was irregular.
- (iv) The relative elastic modulus of the Schwarz-P structure can be expressed by the Gibson-Ashby model as a function of the theoretical relative density ρ_p/ρ_s : $E_p/E_s = 0.31(\rho_p/\rho_s)^{1.76}$. In addition, the fractured surface consisted of a mixture of smooth planes and micro-

sized dimples, exhibiting a mixed ductile and brittle failure mode.

Acknowledgments

The authors would like to express their sincere appreciation to Mr. He Junjie, PhD candidate, from Tokyo University of Agriculture and Technology for his support on the analysis of the microstructure.

Funding

None.

Conflict of interest

The authors declare that they have no known competing financial interests or personal relationships that could have appeared to influence the work reported in this paper.

Author contributions

Conceptualization: Shujie Tan, Yicha Zhang

Formal analysis: Ziyu Wang

Funding acquisition: Liping Ding

Investigation: Shujie Tan, Xi Zhang

Methodology: Shujie Tan, Liping Ding, Yicha Zhang

Project administration: Wenliang Chen

Visualization: Xi Zhang

Writing – original draft: Shujie Tan, Xi Zhang

Writing – review & editing: Yicha Zhang

References

1. Maconachie T, Leary M, Lozanovski B, *et al.*, 2019, SLM lattice structures: Properties, performance, applications and challenges. *Mater Design*, 183: 108137.
<https://doi.org/10.1016/j.matdes.2019.108137>
2. McGregor M, Patel S, McLachlin S, *et al.*, 2021, Architectural bone parameters and the relationship to titanium lattice design for powder bed fusion additive manufacturing. *Addit Manuf*, 47: 102273.
<https://doi.org/10.1016/j.addma.2021.102273>
3. Feng J, Fu J, Yao X, *et al.*, 2022, Triply periodic minimal surface (TPMS) porous structures: From multi-scale design, precise additive manufacturing to multidisciplinary applications. *Int J Extrem Manuf*, 4: 022001.
4. Du Plessis A, Broeckhoven C, Yadroitsava I, *et al.*, 2019, Beautiful and functional: A review of biomimetic design in additive manufacturing. *Addit Manuf*, 27: 408–427.
<https://doi.org/10.1016/j.addma.2019.03.033>
5. Pham MS, Liu C, Todd I, *et al.*, 2019, Damage-tolerant architected materials inspired by crystal microstructure. *Nature*, 565: 305–311.
<https://doi.org/10.1038/s41586-018-0850-3>

6. Thompson MK, Moroni G, Vaneker T, *et al.*, 2016, Design for additive manufacturing: Trends, opportunities, considerations, and constraints. *CIRP Ann Manuf Technol*, 65: 737–760.
7. Vaneker T, Bernard A, Moroni G, *et al.*, 2020, Design for additive manufacturing: Framework and methodology. *CIRP Annals*, 69: 578–599.
<https://doi.org/10.1016/j.cirp.2020.05.006>
8. Zhang Y, Yang S, Zhao YF, 2020, Manufacturability analysis of metal laser-based powder bed fusion additive manufacturing—a survey. *Int J Adv Manuf Technol*, 110: 57–78.
9. Shi Y, Zhang Y, Baek S, *et al.*, 2018, Manufacturability analysis for additive manufacturing using a novel feature recognition technique. *Comput Aided Design Appl*, 15: 941–952.
<https://doi.org/10.1080/16864360.2018.1462574>
10. Yang L, Yan C, Cao W, *et al.*, 2019, Compression-compression fatigue behaviour of gyroid-type triply periodic minimal surface porous structures fabricated by selective laser melting. *Acta Mater*, 181: 49–66.
<https://doi.org/10.2139/ssrn.3406935>
11. Yan X, Yue S, Ge J, *et al.*, 2022, Microstructural and mechanical optimization of selective laser melted Ti6Al4V lattices: Effect of hot isostatic pressing. *J Manuf Processes*, 77: 151–162.
<https://doi.org/10.1016/j.jmapro.2022.02.024>
12. Ding J, Zou Q, Qu S, *et al.*, 2021, STL-free design and manufacturing paradigm for high-precision powder bed fusion. *CIRP Annals*, 70: 167–170.
<https://doi.org/10.1016/j.cirp.2021.03.012>
13. Feng J, Fu J, Lin Z, *et al.*, 2019, Layered infill area generation from triply periodic minimal surfaces for additive manufacturing. *Comput Aided Design*, 107: 50–63.
<https://doi.org/10.1016/j.cad.2018.09.005>
14. Feng J, Fu J, Shang C, *et al.*, 2020, Efficient generation strategy for hierarchical porous scaffolds with freeform external geometries. *Addit Manuf*, 31: 100943.
<https://doi.org/10.1016/j.addma.2019.100943>
15. Ding L, Tan S, Chen W, *et al.*, 2021, Manufacturability analysis of extremely fine porous structures for selective laser melting process of Ti6Al4V alloy. *Rapid Prototyp J*, 27: 1523–1537.
<https://doi.org/10.1108/RPJ-11-2020-0280>
16. Ding L, Tan S, Chen W, *et al.*, 2022, Development of a manufacturability predictor for periodic cellular structures in a selective laser melting process via experiment and ANN modelling. *Virtual Phys Prototyp*, 17: 948–965.
<https://doi.org/10.1080/17452759.2022.2091461>
17. Yan C, Hao L, Hussein A, *et al.*, 2012, Evaluations of cellular lattice structures manufactured using selective laser melting. *Int J Mach Tools Manuf*, 62: 32–38.
<https://doi.org/10.1016/j.ijmactools.2012.06.002>
18. Yan C, Hao L, Hussein A, *et al.*, 2014, Advanced lightweight 316L stainless steel cellular lattice structures fabricated via selective laser melting. *Mater Design*, 55: 533–541.
<https://doi.org/10.1016/j.matdes.2013.10.027>
19. Neikter M, Huang A, Wu X, 2019, Microstructural characterization of binary microstructure pattern in selective laser-melted Ti-6Al-4V. *Int J Adv Manuf Technol*, 104: 1381–1391.
20. Zhang Y, Tan S, Ding L, *et al.*, 2021, A toolpath-based layer construction method for designing & printing porous structure. *CIRP Annals*, 70: 123–126.
<https://doi.org/10.1016/j.cirp.2021.04.020>
21. Tan S, Zhang X, Ding L, *et al.*, 2021, An Efficient Layer Construction Method to Generate Accurate Printing Toolpaths of Periodic Cellular Structures for Selective Laser Melting Process Solid Freeform Fabrication 2021. In: *Proceedings of the 32th Annual International Solid Freeform Fabrication Symposium*.
22. International Organization for Standardization. Mechanical Testing of Metals-Ductility Testing-compression Test for Porous and Cellular Metals. Geneva: International Organization for Standardization. ISO 13314-2011.
23. Ashby MF, 2006, The properties of foams and lattices. *Philos Trans A Math Phys Eng Sci*, 364: 15–30.
<https://doi.org/10.1098/rsta.2005.1678>
24. Zhao X, Li S, Zhang M, *et al.*, 2016, Comparison of the microstructures and mechanical properties of Ti-6Al-4V fabricated by selective laser melting and electron beam melting. *Mater Design*, 95: 21–31.
<https://doi.org/10.1016/j.matdes.2015.12.135>
25. Chang C, Huang J, Yan X, *et al.*, 2020, Microstructure and mechanical deformation behavior of selective laser melted Ti6Al4V ELI alloy porous structures. *Mater Lett*, 277: 128366.
<https://doi.org/10.1016/j.matlet.2020.128366>
26. Vrancken B, Thijs L, Kruth JP, *et al.*, 2012, Heat treatment of Ti6Al4V produced by selective laser melting: Microstructure and mechanical properties. *J Alloys Compds*, 541: 177–185.
<https://doi.org/10.1016/j.jallcom.2012.07.022>